



Quasi-geostrophic vortex merger over bathymetry

Jean N. Reinaud¹ , Joseph H. LaCasce²  and Xavier J. Carton³

¹School of Mathematics and Statistics, University of St Andrews, St Andrews KY169SS, UK

²Department of Geosciences, Univ of Oslo, Oslo 0315, Norway

³LOPS/IUEM/UBO, rue Dumont D'Urville, Plouzané 29280, France

Corresponding author: Jean N. Reinaud, jnr1@st-andrews.ac.uk

(Received 13 December 2024; revised 3 September 2025; accepted 9 September 2025)

We investigate interactions between two like-signed vortices over either an isolated seamount or a basin (a depression in the bathymetry), using a quasi-geostrophic, two-layer model on the f -plane. When the vortex pair is centred over the seamount, the vortices are pushed together by the secondary flow generated in the bottom layer, facilitating their merger. Over a basin, the deep anomalies are much stronger and their interaction strains out the surface vortices. The results are supported by an analytical estimation of the initial potential vorticity anomalies in the lower layer and by analysis of the linear stability of a single vortex over the bathymetry. Similar phenomena are observed when the vortex pair is displaced from the bathymetric centre and when the initial vortices are initially compensated. Sub-deformation-scale vortices are less influenced by bathymetry than larger vortices. The results help explain asymmetries noted previously in turbulence simulations over bathymetry.

Key words: quasi-geostrophic flows, topographic effects, vortex dynamics

1. Introduction

Vortices are masses of fluid in rotation and are key dynamical features in the oceans (Carton 2001), at the surface (Chelton, Schlax & Samelson 2011) and in the interior (e.g. Petersen *et al.* 2013). Among these, ‘mesoscale vortices’ are those whose horizontal size is comparable to the Rossby deformation radius, of order 20 km. These are among the most energetic features in the oceans (e.g. Grooms, Nadeau & Smith 2013; Byrne *et al.* 2016; Hidenori, Xiaoming & Greatbatch 2016). The vortices typically have modest Rossby numbers, so they are amenable to study with a quasi-geostrophic dynamics (Vallis 2006).

Vortices interact strongly with their surroundings: with other vortices, with currents and jets, with coasts and with bathymetry. The present paper focuses on the latter. We are specifically interested in mergers between like-signed vortices over isolated features, seamounts and depressions.

Vortex merger is an important elementary interaction. It is associated with the inverse energy and direct enstrophy cascades in large-scale geophysical flows. By merging, vortices form larger structures, contributing in physical space to the inverse energy cascade in spectral space. Mergers also generate filaments (and, occasionally, low-energy, small-scale vortices), contributing to the direct cascade of enstrophy. Vortex merger has thus been the subject of numerous studies. It was first investigated numerically in a two-dimensional incompressible flow by Roberts & Christiansen (1972) and Rossow (1977). It was shown that vortices merge provided they are closer than a critical distance. Overman & Zabusky (1982) demonstrated that the merger of two co-rotating patches of uniform vorticity in mutual equilibrium can be linked to an instability of the co-rotating vortex pair, as suggested by Saffman & Szeto (1980) (see also Dritschel 1995). Mergers in viscous two-dimensional flows have been studied (Meunier *et al.* 2002; Cerretelli & Williams 2003), as have mergers in quasi-geostrophic, two-layer models (e.g. Polvani, Zabusky & Flierl 1989), with the so-called ‘surface quasi-geostrophic’ model (Carton *et al.* 2016), and in three-dimensional, continuously stratified, quasi-geostrophic flow (von Hardenberg *et al.* 2000; Dritschel 2002; Reinaud & Dritschel 2005; Bambrey, Reinaud & Dritschel 2007; Ozurgurlu, Reinaud & Dritschel 2008). Mergers have also been studied with finite Froude and Rossby numbers, where an asymmetry between the merger of cyclonic and anticyclonic vortices is observed (Reinaud & Dritschel 2018). An external shear facilitates mergers between like-signed vortices and impedes mergers otherwise (Carton, Maze & Legras 2002; Trieling, Dam & van Heijst 2010; Reinaud 2017). Mergers over a planar bathymetric slope have also been studied in single (Carton *et al.* 2017) and two-layer flows (de Marez *et al.* 2017).

Bathymetry has significant effects on vortices, see e.g. Zavala Sansón & Gonzalez (2021). An axisymmetric seamount can stabilise a surface cyclone and destabilise an anticyclone, and the opposite occurs over a depression (Benilov 2005; Zhao, Chieusse-Gérard & Flierl 2019; Gonzalez & Zavala Sansón 2023). Isolated cyclones can self-propel up a seamount while anticyclones move off (Carnevale *et al.* 1991a). Turbulent flow over bathymetry can produce mean flows which are ‘prograde’, i.e. parallel to the direction of topographic wave propagation: cyclonic in a basin and anticyclonic over a seamount (Bretherton & Haidvogel 1976; Salmon, Holloway & Hendershott 1976). With stratification, the flow is bottom intensified, with larger vertical extent for bathymetric features larger than the deformation scale (Hogg 1973; Merryfield 1998; Venaille 2012; LaCasce, Palóczy & Trodahl 2024). With a turbulent, barotropic initial state, the result is often a topography-following prograde flow plus an isolated and oppositely signed vortex in the centre (Solodoch, Stewart & McWilliams 2021; Siegelman & Young 2023). With stratification, one can obtain a bottom-intensified prograde flow and an opposite-signed vortex at the surface (de Marez, Le Corre & Gula 2021; LaCasce *et al.* 2024). The lone vortex is evidently the result of an asymmetry in mergers.

The present goal is to investigate this merger asymmetry. We examine the evolution of two displaced vortices over axisymmetric basins and seamounts (hereafter referred to as circular basins and seamounts) and elliptical basins and seamounts. The results confirm that the merger of cyclones/anticyclones is favoured over a seamount/basin, while the opposite-signed vortices are sheared out. The asymmetry is intimately linked to surface vortex stability, in line with Benilov (2005) and Zhao *et al.* (2019).

The paper is organised as follows. Section 2 introduces the equations, initial conditions and numerical method. Section 3 presents the main results. The results are analysed in terms of potential vorticity (PV) anomalies induced in the lower layer, and of the stability of a single vortex. We then consider various effects, including (i) basin asymmetry, (ii) vortex scale relative to the deformation radius, (iii) the alignment of vortices and bathymetry and (iv) the initial flow in the lower layer. Conclusions are presented in § 4.

2. Methods

We consider a quasi-geostrophic (QG) two-layer flow over bathymetry. The bathymetric height is denoted $h_b(x, y)$. We assume the Coriolis frequency is constant, $f = f_0$, for simplicity. The QG flow is fully described by the PVs, $q_i(x, y, t)$, in each layer $i = 1, 2$; these are defined from the streamfunction, φ_i , $i = 1, 2$ as

$$q_1 = \nabla^2 \varphi_1 - \gamma_1^2 (\varphi_1 - \varphi_2), \quad (2.1)$$

$$q_2 = \nabla^2 \varphi_2 - \gamma_2^2 (\varphi_2 - \varphi_1) + \alpha_b h_b; \quad (2.2)$$

(Vallis 2006). We make the ‘rigid lid’ assumption and neglect deflections of the sea’s surface, which play a minor role at these scales. Layer $i = 1$ corresponds to the upper layer while $i = 2$ to the bottom layer. The bathymetry lies fully in layer 2. Furthermore, $\nabla^2 = \partial^2/\partial x^2 + \partial^2/\partial y^2$ is the horizontal Laplacian, and

$$\gamma_i = \frac{f_0}{\sqrt{g'H_i}} \quad \alpha_b = \frac{f_0}{H_2}, \quad (2.3)$$

where H_i is the mean depth of layer i and $g' \equiv g\Delta\rho/\rho_0$ is the reduced gravity, with $\Delta\rho \equiv \rho_2 - \rho_1$ the density difference between the two layers and $\rho_0 = (\rho_1 + \rho_2)/2$ the mean density. For simplicity we set $H_1 = H_2 = H$, hence $\gamma_1 = \gamma_2 = \gamma \equiv R_d^{-1}$, where R_d is the Rossby deformation radius. The advecting geostrophic velocity field derives from the streamfunction φ_i

$$(u_i, v_i) = \left(-\frac{\partial \varphi_i}{\partial y}, \frac{\partial \varphi_i}{\partial x} \right), \quad i = 1, 2. \quad (2.4)$$

In the absence of frictional and dissipative effects, the PVs are materially conserved on the f -plane

$$\begin{aligned} \frac{Dq_1}{Dt} &= 0, \\ \frac{Dq_2}{Dt} &= 0. \end{aligned} \quad (2.5)$$

In layer 2, we also define the PV anomaly

$$q_2^a \equiv q_2 - \alpha_b h_b = \nabla^2 \varphi_2 - \gamma^2 (\varphi_2 - \varphi_1). \quad (2.6)$$

The PV anomaly q_2^a is not materially conserved. For simplicity we hereafter refer to the fields q_1 and q_2^a as PV anomalies.

We solve the equations numerically using a pseudo-spectral method. Some details are provided in Appendix A. Equations (2.5) are advanced in time using a second-order, semi-implicit, leapfrog integration scheme. For numerical stability, weak bi-harmonic diffusion is added to the right-hand side of (2.5), with a hyperviscosity coefficient $\nu = 2 \times 10^{-9}$.

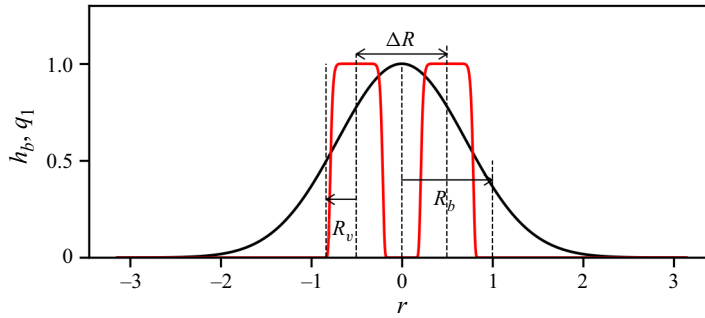


Figure 1. Geometry of the initial conditions. Bathymetry (Gaussian seamount) of characteristic radius $h_b(x, y)$ with $R_b = 3R_d = 1$ (black). The PV field in the upper layer q_1 at $t = 0$ for $R_v = R_d$ and $\Delta R = 3R_d$ (red).

The time step is $\Delta t = K 2\pi / (Nu_{max})$, where we use a Courant-Friedrichs-Lewy (CFL) coefficient of $K = 0.1$ for higher accuracy, where u_{max} is the maximum velocity at $t = 0$. This choice of K also proved, in practice, to provide numerical stability to the leapfrog scheme. Fields in spectral space are dealiased using the 2/3-rule. A note on numerical convergence is provided in [Appendix A](#).

By the symmetry of the QG equations on the f -plane, the evolution of cyclonic vortices over a seamount (or a basin) is equivalent to that of anticyclonic vortices over a basin (or a seamount). We therefore restrict our attention to cyclonic vortices in the upper layer and consider both a basin and a seamount. The initial conditions are given by

$$q_1(x, y, 0) = q_0 e^{-8 \left(\frac{(x-x_{c,1})^2 + (y-y_{c,1})^2}{R_v^2} \right)} + q_0 e^{-8 \left(\frac{(x-x_{c,2})^2 + (y-y_{c,2})^2}{R_v^2} \right)}, \quad (2.7)$$

$$q_2^a(x, y, 0) = 0, \quad (2.8)$$

$$h_b(x, y) = h_0 e^{-(x/d_x)^2 - (y/d_y)^2}, \quad (2.9)$$

where $(x_{c,j}, y_{c,j})$ is the centre of vortex j at $t = 0$, R_v is the common characteristic radius of the two vortices in the upper layer and q_0 is their common maximum PV. Although the details of the interaction between two vortices depend on their initial shape and their PV distribution, circular vortices are representative of generic vortices and allow investigation of the influence of bathymetry on vortex mergers. We set $q_0 = 1$. This sets the problem time scale. For example, in the limit $\gamma \rightarrow 0$, a uniform PV axisymmetric vortex has a turnover period of $T = 4\pi/q_0 = 4\pi$. The bathymetry consists of a single elliptical Gaussian seamount/basin of length d_x in the x -direction and d_y in the y -direction, and maximal height h_0 . Circular bathymetry has $d_x = d_y$. The topographic height is varied, but we use $h_0 = \pm 1 = \alpha_b^{-1}$ for a seamount and basin, respectively, such that $\alpha_b h_0 = \pm q_0$ unless stated otherwise. The initial vortex spacing is $\Delta R \equiv \sqrt{(x_{c,2} - x_{c,1})^2 + (y_{c,2} - y_{c,1})^2}$.

The vortex radius is $R_v = R_d$, unless stated otherwise. The vortices are, however, always kept small compared with the domain, to limit the effects of the periodic boundary conditions in the horizontal directions. Note too that, despite the vortex PV distributions being physically separate, the streamfunctions overlap; thus the vortices interact. [Figure 1](#) illustrates the geometry of the initial condition for a circular seamount with $d_x = d_y = R_b = 3R_d$.

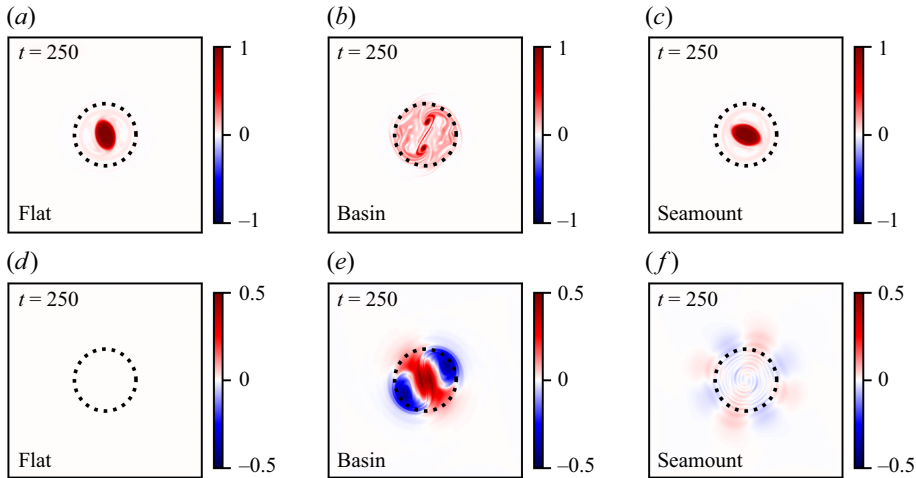


Figure 2. Potential vorticity anomalies at $t = 250$ for deformation-scale vortices ($R_v = R_d$) with an initial separation of $\Delta R = 2R_v$. Top row: q_1 for (a) a flat bathymetry, (b) a circular basin and (c) a circular seamount. Bottom row: q_2^a for (d) a flat bathymetry, (e) a circular basin and (f) a circular seamount.

The problem has four non-dimensional parameters: the initial distance between the two vortices, the vortex radius, the bathymetry characteristic radius and the bathymetry height. The main focus of the paper is on the effect of the first two parameters. We also conduct additional numerical experiments to explore the effects of the radius and height of the bathymetry.

3. Results

3.1. Circular bathymetry

We first consider a circular seamount/basin with $d_x = d_y = R_b = 3R_d$. We define a global topographic beta, $\beta_t = f_0 h_0 / (R_b H) = \alpha_b h_0 / R_b = \pm 1$ for the seamount/basin. The vortex radius is set to the Rossby deformation radius so that $R_v = R_d$, and the initial spacing is $\Delta R = 2R_v$ at $t = 0$.

Figure 2 shows the PV anomalies q_1 and q_2^a at $t = 250$ for a basin (panels *a* and *d*), a flat bottom (*b* and *e*) and a seamount (*c* and *f*). With the flat bottom, q_2^a remains zero, as expected. In all three cases, the vortices in the upper layer merge. With the flat bottom or seamount, the merged vortices shed a small amount of filamentary PV. But with the basin, the vortices have been almost completely strained out. What remains is an intricate pattern of filamentary PV and two small PV cores. At the same time, the lower-layer PV anomaly, q_2^a , has organised into a tripole, with cyclonic PV at the basin centre and anticyclonic vortices on the side. The vortices have strong associated surface flows and these stir the surface PV. A similar erosion of an anticyclonic vortex over a seamount was described by Herbertte, Morel & Arhan (2003). Finally, the q_2^a -pattern observed in figure 2(*f*) resembles one of the linear trapped Rossby waves obtained by Zavala Sansón (2010).

The evolution of the maximum and minimum PV anomalies at depth, i.e. $|q_{2,m}^-| = |\min_{\text{domain}} q_2^a|$ and $q_{2,m}^+ = \max_{\text{domain}} q_2^a$, are shown in panel (a) of figure 3 for the basin and seamount cases. The initial increase in both cases is similar. Over the seamount, the maximum plateaus to a value 6.6 % times the surface maximum, q_0 , but over the basin, the values increase much more, to approximately ~ 47 % of q_0 , reflecting the formation of the deep tripole.

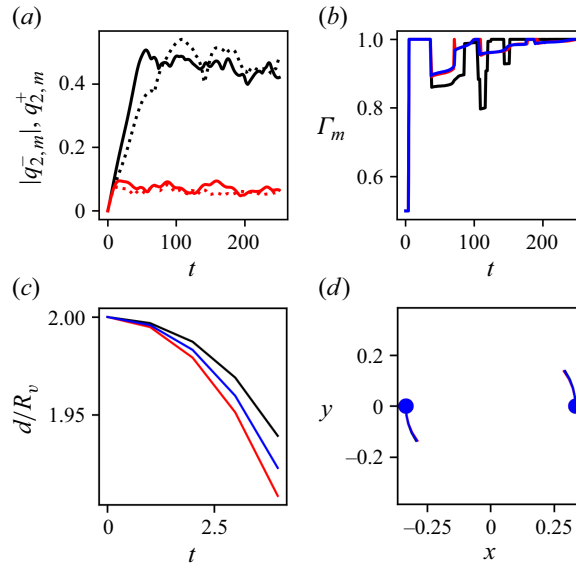


Figure 3. Evolution of (a) the maximal PV anomaly in the bottom layer (in absolute value) $|q_{2,m}^-|$ (solid lines) and $q_{2,m}^+$ (dotted lines) for $R_v = R_d$ and $\Delta R = 2R_v$, for a basin (black) and a seamount (red); (b) surface circulation, Γ_m , of the PV anomaly q_1 of the largest vortex over the total circulation of all vortices Γ_{tot} for a circular basin (black), a circular seamount (red) and a flat bottom (blue); (c) distance between the centres of the two largest vortices of the upper layer (same colours as in panel (b)); (d) trajectory of the vortex centres (same colours as in panel (b) and the circles denote the initial vortex centre locations).

Shown in figure 3(b) is the integrated surface PV anomaly of the largest coherent structure divided by the sum of the same quantity over all structures in the upper layer, denoted Γ_m . A coherent structure is defined as a region of contiguous PV in excess of the root-mean-square value over the computational domain. A unit value of Γ_m indicates there is only one coherent structure present. At $t = 0$, $\Gamma_m = 0.5$ as there are two identical vortices in the upper layer. As the vortices merge, $\Gamma_m \rightarrow 1$. The figure shows the vortices merge very rapidly, by $t \simeq 5$, in all three cases (basin, flat bathymetry, seamount). From time to time, filaments detach from the main vortex, causing Γ_m to decrease below one; but it returns to one as the filaments are either reabsorbed or dissipated. Note $\Gamma_m \simeq 1$ at $t = 250$ also for the basin; thus the mixture of filaments and small vortices by this measure is like a highly deformed single structure.

Having identified the coherent structures, we can determine their geometric centres. Figure 3(c) shows the evolution of the distance between the two vortex centres until they merge at $t \simeq 4$. The results indicate the merger is faster/slower over the seamount/basin than over a flat bottom. Panel (d) shows the trajectory of the centres in the upper layer until they merge. These are visually indistinguishable in the three cases.

The early evolution of the PV for the basin is shown in figure 4 while figure 5 shows the same fields over the seamount. In both cases, q_2^a exhibits a quadrupole structure initially, i.e. azimuthal mode $m = 2$. The pattern is reminiscent of seamount-trapped waves (Brink 1990; Haidvogel *et al.* 1993), but the propagation direction differs, being counter-clockwise over both bathymetries. Shortly thereafter the evolutions differ. Over the basin, the cyclonic lobes merge and settle in the basin centre while the anticyclonic lobes circle as satellites, and the resulting tripole intensifies. With the seamount this never happens; instead, the deep quadrupole strains out and fails to intensify.

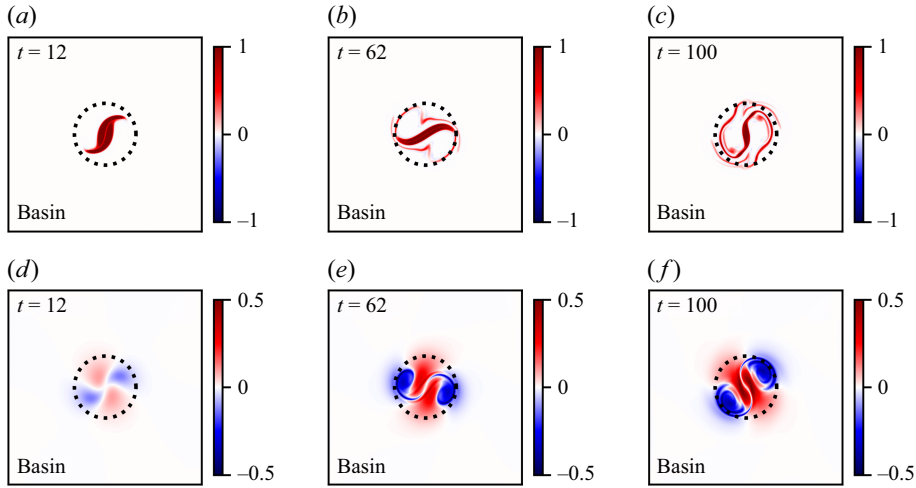


Figure 4. Potential vorticity anomalies for the circular basin case at earlier times, with $R_v = R_d$ and $\Delta R = 2R_v$. Top row: q_1 at (a) $t = 12$, (b) $t = 62$ and (c) $t = 100$. Bottom row: q_2^a at (d) $t = 12$, (e) $t = 62$ and (f) $t = 100$.

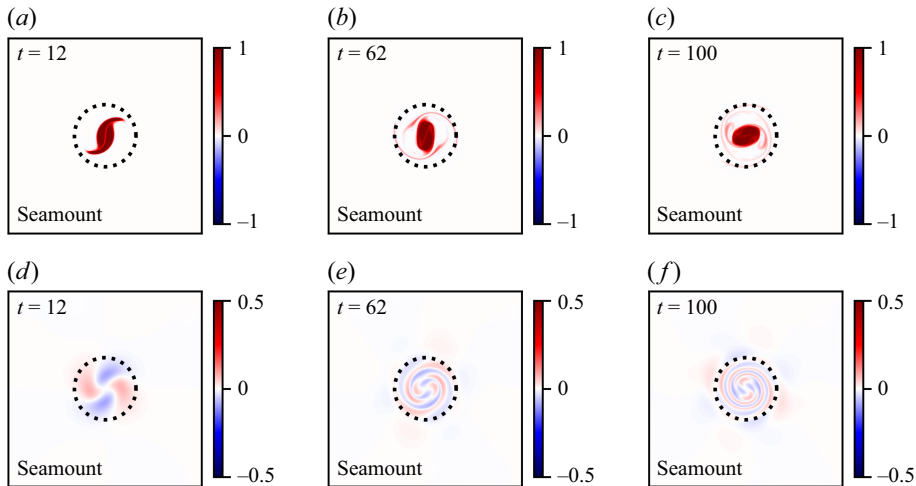


Figure 5. Potential vorticity anomalies for the circular seamount at earlier times, with $R_v = R_d$ and $\Delta R = 2R_v$. Top row q_1 at (a) $t = 12$, (b) $t = 62$ and (c) $t = 100$. Bottom row q_2^a at (d) $t = 12$, (e) $t = 62$ and (f) $t = 100$.

The deep tripole has no expression in the surface PV (as seen by the two blank regions in surface PV in figure 4(b,c). This is as expected for topographic waves in two layers (LaCasce 1998; LaCasce *et al.* 2024). However, the features do have surface flow, and the strength of topographic wave surface flow depends on the wavelength; if comparable to the deformation radius (as here), the flow approaches the bottom flow in strength. The result is a strong interaction between the deep and surface anomalies. The effect is absent over the seamount on the other hand. The merged vortex persists, gradually becoming more axisymmetric.

Figure 6 shows the same PV diagnostics as in figure 3 but with a greater initial vortex separation ($\Delta R = 3R_v$). Here, differences over the three types of bathymetry are even

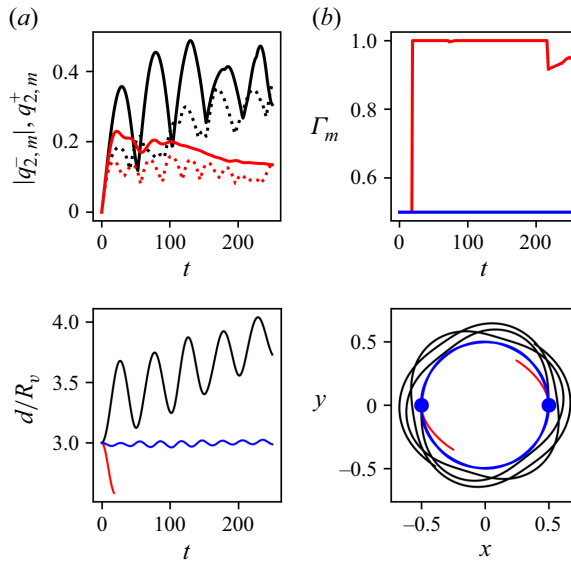


Figure 6. Evolution of (a) the maximal PV anomaly in the bottom layer (in absolute value) $|q_{2,m}^-|$ and $q_{2,m}^+$ for $R_v = R_d$, $\Delta R = 3R_v$, with a circular basin (black) and a circular seamount (red); (b) surface circulation, Γ_m , of q_1 of the largest vortex over the total circulation of all vortices Γ_{tot} for a basin (black), a seamount (red) and a flat bathymetry (blue); (c) distance between the centres of the two largest vortices of the upper layer (same colours as in panel (b)); (d) trajectory of the vortex centres (same colours as in panel (b) and the circles denote the initial vortex centre locations).

more pronounced. While the surface vortices merge over the seamount (red curves in panels *c* and *d*), the vortices over a flat bottom and basin co-rotate without merging (blue and black curves). Indeed, in the latter case the vortices slowly migrate away from each other. The fraction of PV in a single structure thus reaches one for the seamount but stays near 0.5 for the other cases (panel *b*). However, as before, the formation of deep PV anomalies is most pronounced over the basin (black curves in panel *a*); it is weaker over the seamount (red curves).

The behaviour for a range of initial separations, ΔR , is summarised in [table 1](#) and illustrated in [figure 7](#). Most significantly, the vortices must be closer than approximately $2.6R_v$ to merge over a basin while they can be as far apart as $3.2R_v$ above a seamount. For reference, the critical merger distance is $2.7R_v$ over a flat bottom. Moreover, the core of the merged vortex is much smaller over a basin than over a seamount, again as a large part of the PV is strained out into filaments.

3.2. Initial production of q_2^a

The generation of the deep anomalies initially can be estimated analytically. To do this, we represent the vortices as two circular regions with uniform PV. We define the barotropic PV, q_b , and the baroclinic PV, q_c , such that

$$q_b = \frac{q_1 + q_2^a}{2}, \quad q_c = \frac{q_1 - q_2^a}{2}. \quad (3.1)$$

The associated barotropic and baroclinic streamfunctions are φ_b and φ_c , such that

$$q_b = \nabla^2 \varphi_b, \quad q_c = \nabla^2 \varphi_c - \gamma^{*2} \varphi_c, \quad (3.2)$$

where $\gamma^* = \sqrt{2}\gamma_1 = \sqrt{2}\gamma_2$, with equal layer depths.

Bathymetry	$\Delta R/R_v$	Evolution in the upper layer
Basin	2.55	Merger at $t \simeq 11$. Partial straining out. A small central vortex remains.
Basin	2.6	Merger at $t \simeq 12$. Merged vortex splits into two vortices at $t \simeq 56$.
Basin	2.7	Merger at $t \simeq 61$, splitting into two vortices at $t \simeq 110$
Basin	2.8	Merger at $t \simeq 60$, then split at $t \simeq 80$.
Basin	2.9	Vortices touch at $t \simeq 53$ to separate immediately.
Basin	2.95	No merger (occasional small filamentary bridge between the vortices).
Flat	2.7	Merger at $t \simeq 14$
Flat	2.75	Merger at $t \simeq 16$, split at $t \simeq 75$. Quasi-periodic merger and splitting afterwards.
Flat	2.8	Merger at $t \simeq 24$, split at $t \simeq 44$. Quasi-periodic touch and separate afterwards.
Flat	2.9	Vortices quasi-periodically touch and separate from $t = 54$.
Flat	2.95	Vortices briefly touch and separate.
Flat	3.0	No merger
Seamount	3.0	Merger at $t \simeq 21$
Seamount	3.05	Merger at $t \simeq 21$, splitting at $t \simeq 63$, merger again at $t \simeq 91$.
Seamount	3.1	Vortices touch at $t = 24$ then separate. Quasi-periodically touch and separate from $t \simeq 118$.
Seamount	3.2	Merger at $t = 97$.
Seamount	3.3	Vortices touch and separate quasi-periodically from $t = 95$.
Seamount	3.4	Vortices touch and separate quasi-periodically from $t = 171$.
Seamount	3.45	No merger.

Table 1. Qualitative descriptions of the evolution of the pair of cyclonic vortices in the upper layer for $R_v = R_d$ over a circular bathymetry for $0 \leq t \leq 250$.

For a single patch of radius R_v of uniform PV q_0 at $(0, 0)$, (3.2) can be inverted to give

$$\varphi_b = \begin{cases} \frac{qb r^2}{4}, & r \leq R_v, \\ \frac{qb R_v}{2} \ln(r/R_v) + \frac{qb}{4}, & r > R_v, \end{cases} \quad (3.3)$$

$$\varphi_c = \begin{cases} \frac{q_c}{\gamma^{*2}} (\gamma^* R_v K_1(\gamma^* R_v) I_0(\gamma^* r) - 1), & r \leq R_v, \\ \frac{q_c}{\gamma^{*2}} (-\gamma^* R_v K_0(\gamma^* r) I_1(\gamma^* R_v)), & r > R_v, \end{cases} \quad (3.4)$$

where K_0 and K_1 are the modified Bessel functions of the second kind for zeroth and first orders, while I_0 and I_1 are the modified Bessel functions of the first kind of zeroth and first orders (e.g. Sokolovskiy & Verron 2014). The associated azimuthal barotropic and baroclinic azimuthal velocities are

$$u_b = \begin{cases} \frac{qb r}{2}, & r \leq R_v, \\ \frac{qb R_v^2}{2r}, & r > R_v, \end{cases} \quad (3.5)$$

$$u_c = \begin{cases} q_c R_v K_1(\gamma^* R_v) I_1(\gamma^* r), & r \leq R_v, \\ q_c R_v K_1(\gamma^* r) I_1(\gamma^* R_v), & r > R_v. \end{cases} \quad (3.6)$$

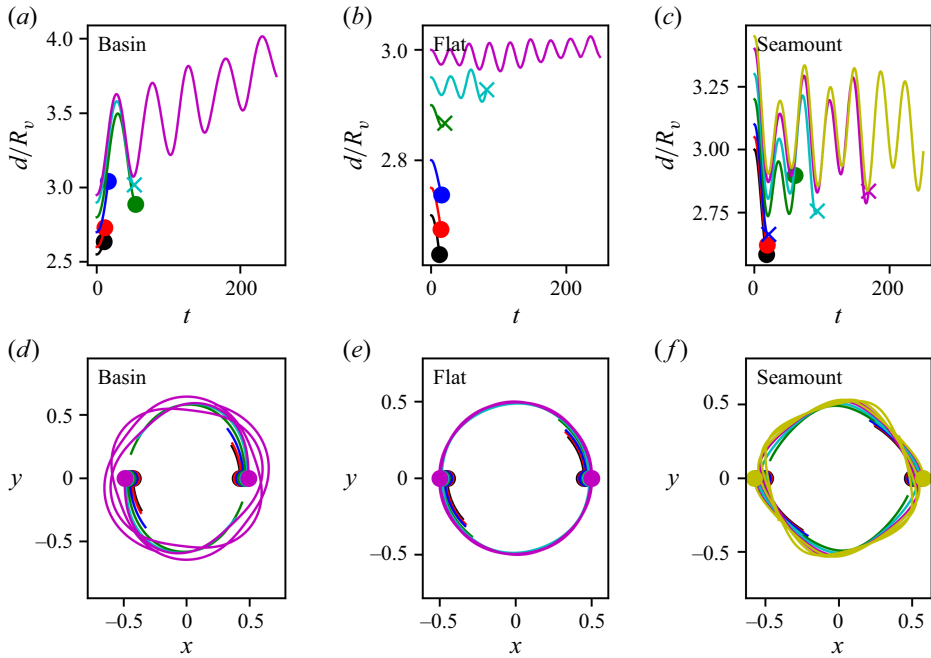


Figure 7. Evolution of the relative distance, d/R_v , between the centres of the upper-layer vortices with $R_v = R_d$ until they first touch for (a) a circular basin and $\Delta R/R_v = 2.55$ (black), 2.6 (red), 2.7 (blue), 2.8 (green), 2.9 (cyan) and 2.95 (magenta); (b) a flat bathymetry and $\Delta R/R_v = 2.7$ (black), 2.75 (red), 2.8 (blue), 2.9 (green), 2.95 (cyan); (c) a circular seamount and $\Delta R/R_v = 3$ (black), 3.05 (red), 3.1 (blue), 3.2 (green), 3.3 (cyan), 3.4 (magenta) and 3.45 (yellow). In panels (a–c) a circle indicates merger and a cross a weaker interaction not leading to merger. Panels (d–f) show trajectories of the vortex centres for a basin and a flat bottom and a seamount, respectively, using the same colour code as panels (a–c). The small circles indicate the initial locations of the centres.

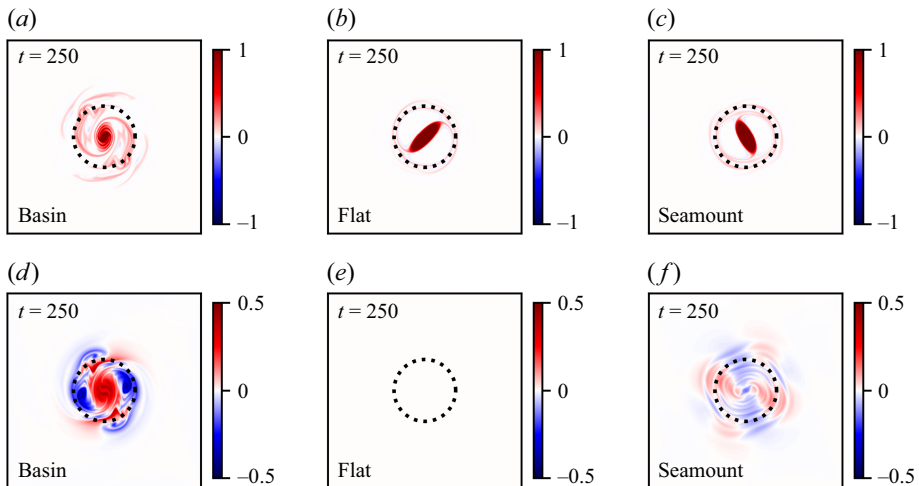


Figure 8. Potential vorticity anomalies at $t = 250$ for $R_v = R_d$. Top row q_1 for (a) a circular basin with $\Delta R = 2.55$, (b) a flat bottom with $\Delta R = 2.7$ and (c) a circular seamount with $\Delta R = 3.0$. Bottom row, q_2^a for (d) a circular basin, (e) flat bottom and (f) a circular seamount.

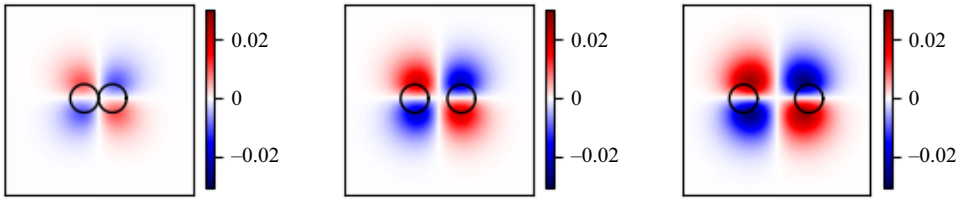


Figure 9. Tendency $\partial q_2^a / \partial t$ at $t = 0$ for two uniform circular patches with $\Delta R = 2R_v$, $3.33R_v$ and $4.67R_v$. The black circles indicate the location of the upper-layer patches. Only the sub-portion of the domain $[-2, 2] \times [-2, 2]$ is shown.

Then, the flow azimuthal velocity induced in the lower layer by the surface vortex is $\mathbf{u}_2 = u_2 \mathbf{e}_\theta$, where

$$u_2 = u_c - u_b = \begin{cases} \frac{q_0}{2} \left(\frac{r}{2} - R_v K_1(\gamma^* R_v) I_1(\gamma^* r) \right), & r \leq R_v, \\ \frac{q_0}{2} \left(\frac{R_v^2}{2r} - R_v K_1(\gamma^* r) I_1(\gamma^* R_v) \right), & r > R_v, \end{cases} \quad (3.7)$$

where \mathbf{e}_θ is the azimuthal unit vector and we have used $q_b = q_c = q_0/2$. By linearity of the equations, the velocity \mathbf{u}_2 induced by two identical circular patches of radius R_v of uniform PV q_0 located at $(\pm d, 0)$ is the sum of the velocities induced by each vortex following (3.7) where r is replaced by $r^\pm = \sqrt{(x \mp d)^2 + y^2}$ and the azimuthal unit vector is defined locally relative to the centre of each vortex. Material conservation of the PV q_2 in layer 2 at $t = 0$ implies that

$$\frac{Dq_2}{Dt} = \frac{\partial q_2^a}{\partial t} + \mathbf{u} \cdot \nabla (\alpha_b h_b) = 0, \quad (3.8)$$

$$\frac{\partial q_2^a}{\partial t} = 2\alpha_b h_b r \mathbf{e}_r \cdot \mathbf{u}_2, \quad (3.9)$$

where \mathbf{e}_r is the radial unit vector.

Figure 9 shows $\partial q_2^a / \partial t$ at $t = 0$ using the same parameters as in § 3.1. This confirms the initial quadrupole pattern seen in § 3.1. It also demonstrates the sensitivity of the intensity of q_2^a to the location of the surface vortices on the slope of the bathymetry.

3.3. Stability of a single vortex

The merged upper-layer vortex also has different stability properties over the bathymetry, as shown by Benilov (2005) and Zhao *et al.* (2019). To see this, we consider a single upper-layer vortex over a Gaussian bathymetry. Again, the vortex is assumed to have uniform PV, q_0 , and radius R_v . We again assume equal layer depths, with $\gamma_1 = \gamma_2 = \gamma$.

The upper vortex is fully described by the radial coordinate of its boundary $r_1(\theta, t)$, with $\bar{r}_1 = R_v$ the basic state vortex radius. The lower-layer PV, a perturbation on the bathymetric contribution, $q_2 = \alpha_0 h_b$, is discretised by N_t circular contours of radius $\bar{r}_{2,i}$, $1 \leq i \leq N_t$, corresponding to constant jumps in q_2 .

The contours of q_1 and q_2 are then perturbed such that

$$r_1(\theta, t) = \bar{r}_1 + \epsilon \operatorname{Re} \left(\eta_1(t) e^{i(m\theta - \sigma t)} \right), \quad (3.10)$$

$$r_{2,i}(\theta, t) = \bar{r}_{2,i} + \epsilon \operatorname{Re} \left(\eta_{2,i}(t) e^{i(m\theta - \sigma t)} \right), \quad (3.11)$$

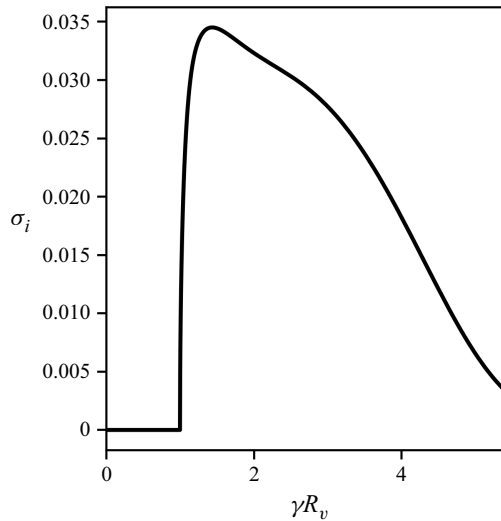


Figure 10. Normalised maximal growth rate σ_i/q_0 vs the normalised vortex radius γR_v for a single uniform PV upper-layer vortex over a Gaussian basin for the perturbation mode of azimuthal wavenumber $m = 2$.

where m is the azimuthal wavenumber of the perturbation and $\epsilon\eta_1, \epsilon\eta_{2mi}$ are the perturbation complex amplitudes, $\sigma = \sigma_r + i\sigma_i$ is the complex frequency and $\text{Re}(\cdot)$ denotes the real part. The imaginary part of σ is the mode's growth rate. The linearised equations for the perturbations $\eta_1, \eta_{2,i}$ yield an eigenvalue problem which we solved numerically. The details of the numerical analysis are given in [Appendix B](#). We set $q_0 = 1$ and $N_t = 8000$.

The maximum growth rate as a function of R_v is plotted in [figure 10](#) for the basin case with $\gamma R_v \in [0, 5.5]$. The largest growth rate corresponds to $\sigma_i/q_0 = 0.0345$ for $\gamma R_v = 1.43$. There is a 'short-wave' cutoff as well, as vortices with $\gamma R_v < 1$ are stable. A similar calculation for the same vortex over a seamount indicates it is neutrally stable.

The nonlinear evolution of a single vortex with $R_v = 0.467$ ($\gamma R_v = 1.4$) is presented in [figure 11](#). The upper vortex has the same PV profile as defined by (2.8) for the two vortex-merger problem. The vortex has uniform PV, smoothed to avoid Gibbs effects in our pseudo-spectral calculation. Mode $m = 2$ is initially excited by making the vortex slightly elliptical, with an aspect ratio of 1.01. As expected, mode $m = 2$ is unstable and the perturbation amplifies. The evolution bears a striking resemblance to that of the merged vortex ([figure 2](#)); a deep tripole forms and the surface cyclone is destroyed.

3.4. Other aspects

3.4.1. Elliptical bathymetry

In turbulent flows, anticyclones trapped over an asymmetric basin are smaller than over a circular one (LaCasce *et al.* 2024). We thus consider mergers between surface cyclones over an elliptical basin and an elliptical seamount. We set $d_x/d_y = 1.5$ while keeping $d_x d_y = 1$ so that the elliptical basin or seamount covers the same area as the circular ones. [Figure 12](#) shows the PV anomaly in both layers at $t = 250$ for both cases, with $\Delta R = 2R_v$ and $R_v = R_d$. The change in bathymetry from circular to elliptical is reflected in the final PV distributions, which are similarly asymmetric and cover the bathymetry.

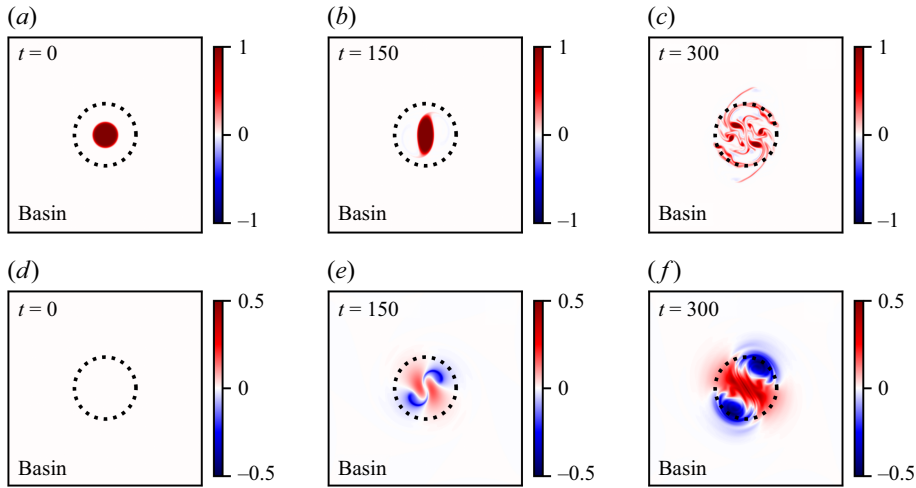


Figure 11. Potential vorticity anomalies for a single vortex of radius $R_v = 1.4R_d$ over a circular basin. Top row, q_1 at (a) $t = 0$, (b) $t = 150$ and (c) $t = 300$. Bottom row, q_2^a for (d) $t = 0$, (e) $t = 150$ and (f) $t = 300$.

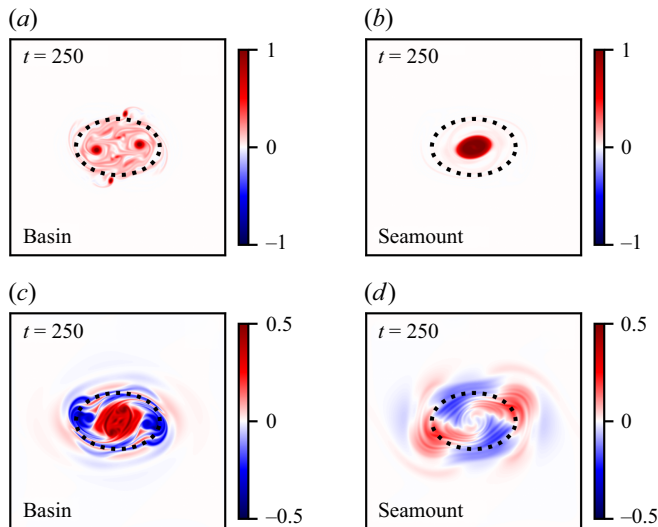


Figure 12. Potential vorticity anomalies at $t = 250$ for $\Delta R = 2R_v$ and $R_v = R_d$. Top row, q_1 for (a) an elliptical basin, (b) an elliptical seamount. Bottom row, q_2^a for (c) an elliptical basin, (d) an elliptical seamount.

Table 2 summarises results from a suite of experiments. Notably, the vortices now interact from further apart, apparently due to the increase in the bathymetric extent in the x -direction. Over the circular basin, the smallest distance for which the vortices do not interact is $\Delta R/R_v = 2.95$ while it is 3.5 for the elliptical basin. The critical separation is larger still for the seamounts, 3.45 for the circular seamount and 4.3 for the elliptical one.

The separation distance d between the vortex centres is plotted in figure 13. The results confirm the vortices interact from further apart when over the elliptical bathymetry. With both a basin and a seamount, the trajectories are more elliptical than in the circular case (panels c, d). The trajectories over the seamount are also more convoluted; this is due to

Bathymetry	$\Delta R/R_v$	Evolution in the upper layer
Basin	2.8	Merger at $t \simeq 17$. Partial straining out. Small central vortex remains.
Basin	2.9	Merger at $t \simeq 22$. Splitting at $t \simeq 48$. New merger $t \simeq 74$. Splitting $t \simeq 100$. Vortices occasionally touch and separate afterwards.
Basin	3.0	Merge at $t \simeq 165$. Splitting at $t \simeq 183$.
Basin	3.1–3.4	Vortices touch and separate.
Basin	3.5	No merger.
Seamount	3.6	Merger at $t \simeq 39$.
Seamount	3.9	Merger at $t \simeq 40$, splitting at $t \simeq 83$ and new merger at $t \simeq 91$.
Seamount	3.9	Megre at $t \simeq 42$, splitting at $t \simeq 79$ and new merger at $t \simeq 96$.
Seamount	3.9	Merger at $t \simeq 48$, splitting at $t \simeq 76$ and new merger at $t \simeq 122$.
Seamount	4.0	Merger at $t \simeq 174$, splitting at 212, about to merger at the end.
Seamount	4.1	Merger at $t \simeq 213$.
Seamount	4.2	Merger at $t \simeq 241$.
Seamount	4.3	Merger at $t \simeq 243$.
Seamount	4.4	Merger at $t \simeq 243$.
Seamount	4.5	No merger by $t = 250$.

Table 2. Qualitative description of the evolution of the pair of cyclonic vortices in the upper layer for $\gamma_1 R_v = \gamma_2 R_v = 1$ over an elliptical bathymetry or an elliptical seamount for $0 \leq t \leq 250$.

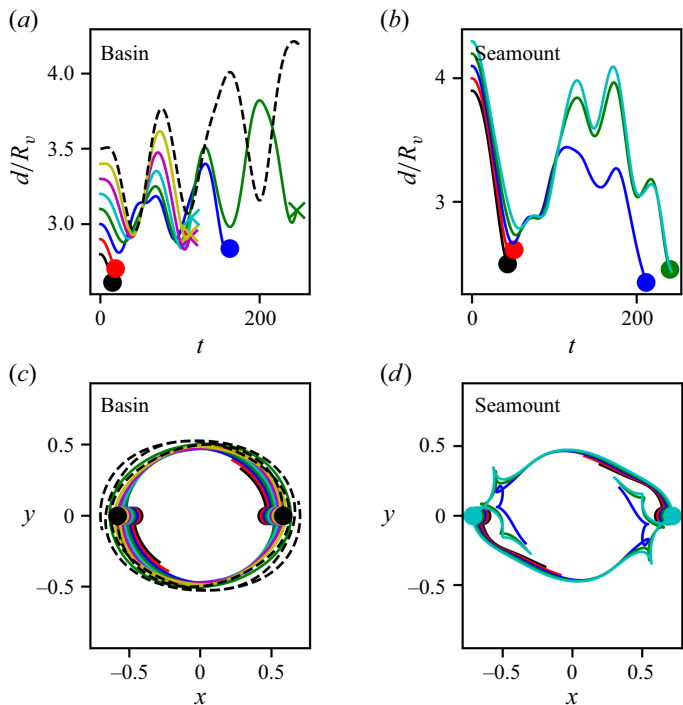


Figure 13. Evolution of the relative distance d/R_v between the centres of the two cyclonic vortices of the upper layer in the case with $R_v = R_d$ until they first touch for (a) an elliptical basin and $\Delta R/R_v = 2.8$ (solid black), 2.9 (solid red), 3.0 (solid blue), 3.1 (solid green), 3.2 (solid cyan), 3.3 (solid magenta), 3.4 (solid yellow) and 3.5 (dashed back); (b) an elliptical seamount and $\Delta R/R_v = 3.9$ (black), 4.0 (red), 4.1 (blue), 4.2 (green) and 4.3 (cyan). In panels (a–b) a circle indicates merger and a cross a weaker interaction not leading to merger. Panels (c–d) show trajectories of the vortex centres for, from left to right, a basin and a seamount using the same colour code as panels (a–b). The small circles indicate the initial locations of the centres.

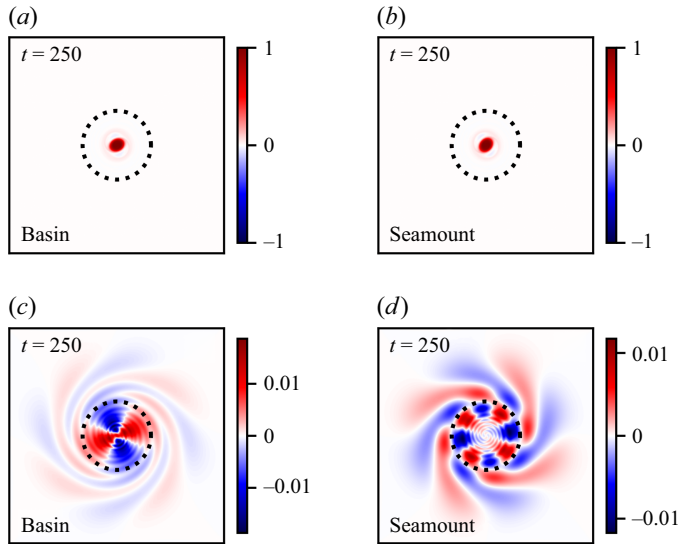


Figure 14. Potential vorticity anomalies at $t = 250$ for $\Delta R = 2R_v$ and $R_v = 0.5R_d$. Top row, q_1 for (a) a circular basin, (b) a circular seamount. Bottom row, q_2^a for (c) a circular basin, (d) a circular seamount.

the formation of multipolar structures in the lower layer which act back on the surface vortices.

3.4.2. Vortex radius

Previously, we focused on deformation-scale vortices. We now investigate varying the vortex radius. We will retain the circular bathymetry as the results are qualitatively the same as over an asymmetric bathymetry.

With vortex radii of half the deformation radius ($\gamma_1 R_v = \gamma_2 R_v = 0.5$) there is much less difference between the basin and seamount (figure 14). Merger occurs over both bathymetries and the flow generated in the lower layer is weak. The energetic tripole for the basin base seen previously is now absent. As inferred from the vortex separations (figure 15), the critical separations for mergers are similar to those with deformation-scale vortices, both for the basin and seamount. The trajectories too are more similar between the bathymetries, indicating less interaction with the deep flows than previously.

On the other hand, the case with larger vortices ($R_v = R_d$) reveals more pronounced asymmetries than with $R_v = R_d$ (figure 16). Merger produces a central vortex over both bathymetries, but the structure is weaker over the basin than over the seamount. Likewise, there is more filamentation over the basin and a strong tripole appears again at depth.

Even when the large vortices do not merge over the basin, there is significant topographic influence. An example, with an initial separation $\Delta R/R_v = 3.2$, is shown in figure 17. The vortices are strongly deformed and an energetic deep flow is generated at depth. This splits into a central cyclonic core and two anticyclonic satellites, and the latter couple with the surface cyclones and translate away. Such baroclinic coupling is an example of a ‘baroclinic modon with a rider’ (Flierl *et al.* 1980), or more commonly a ‘heton’ (Hogg & Stommel 1985). The result is that the cyclones are ejected from over the bathymetry, leaving a predominantly cyclonic circulation in the basin.

These results are in line with sub-deformation-scale vortices being stable over bathymetry and for cyclones over a seamount (§ 3.3). The merger of two half-deformation-scale vortices is accordingly similar over the basin and seamount, while with radii equal to or larger than the deformation radius, a strong tripole appears at depth following an

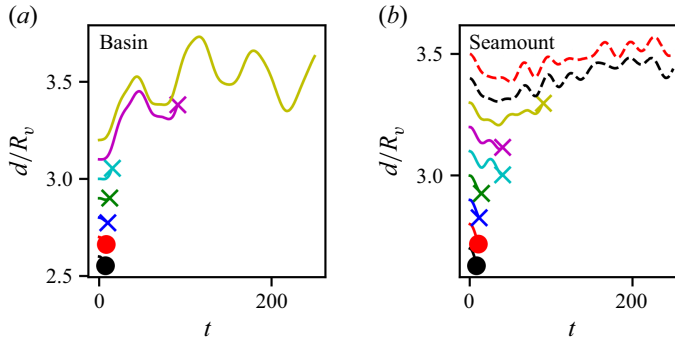


Figure 15. Evolution of the relative distance d/R_v between the centres of the two cyclonic surface vortices with $R_v = 0.5R_d$ until they first touch for (a) a circular basin and $\Delta R/R_v = 2.6$ (black), 2.7 (red), 2.8 (blue), 2.9 (green), 3.0 (cyan), 3.1 (magenta), 3.2 (yellow); (b) a circular seamount and $\Delta R/R_v = 2.7$ (black), 2.8 (red), 2.9 (blue), 3.0 (green), 3.1 (cyan), 3.2 (magenta), 3.3 (yellow), 3.4 (dashed black), 3.5 (dashed red). In panels (a–b) a circle indicates merger while a cross indicates a weaker interaction not leading to merger.

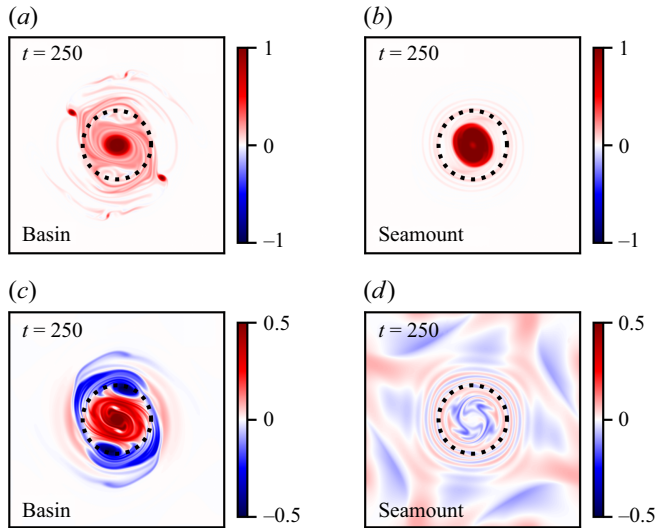


Figure 16. Potential vorticity anomalies at $t = 250$ for $\Delta R = 2R_v$ and $R_v = 1.5R_d$. Top row, q_1 for (a) a circular basin, (c) a circular seamount. Bottom row, q_2^a for (c) a circular basin, (d) a circular seamount at the same time.

$m = 2$ instability. Thus strong bathymetric interactions occur only when the vortices are deformation scale or larger.

3.4.3. Horizontal offset

The previous examples began with vortices placed symmetrically over the bathymetry, but this does not change the qualitative evolution. Here, one vortex is placed over the bathymetric centre and the other is displaced relative to that. We revert to circular bathymetry and deformation-scale vortices ($\gamma_1 R_v = \gamma_2 R_v = 1$).

An example, with $\Delta R = 2R_v$, is shown in figure 18. The primary difference from the aligned case (figure 2) is that the deep vortices are now asymmetric. The tripole is gone, replaced by a distorted dipole. However, the anomalies are comparably strong, indicating a

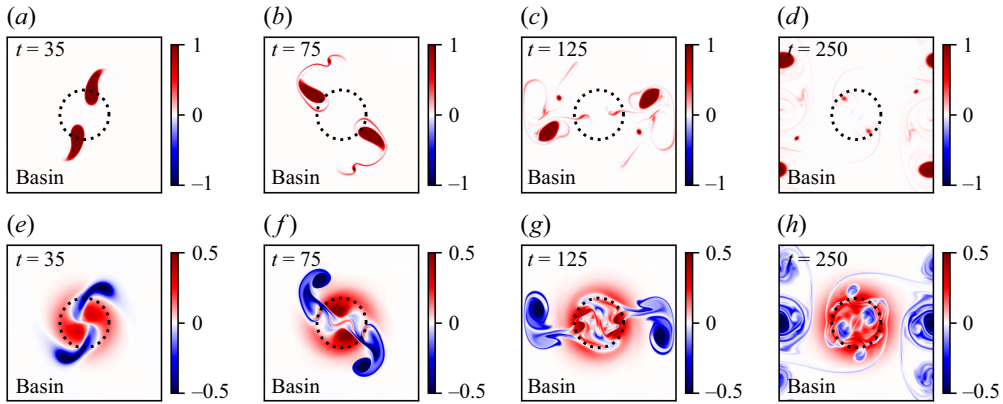


Figure 17. Potential vorticity anomalies with $\Delta R/R_v = 3.2$ and $R_v = 1.5R_d$ over a basin. Top row: q_1 at the times indicated in the panels, bottom row: q_2^a .

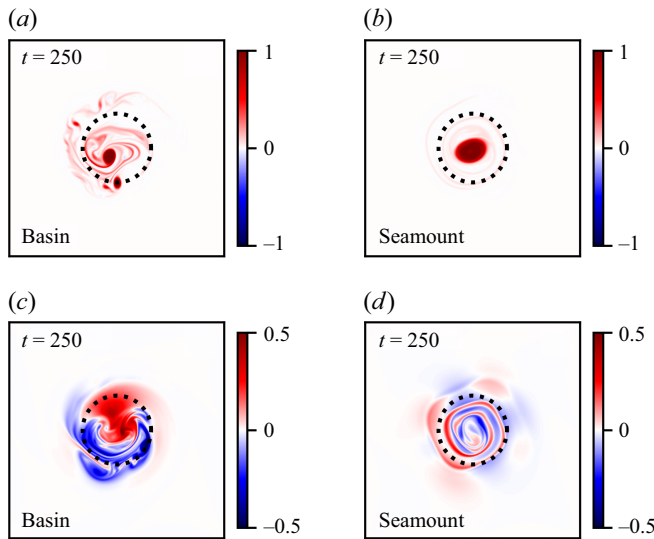


Figure 18. Potential vorticity anomalies at $t = 250$ with $\Delta R = 2R_v$ for an offset pair of vortices and $R_v = R_d$. Top row: q_1 for (a) a circular basin, and (b) a circular seamount. Bottom row: q_2^a for (c) a circular basin, and (d) a circular seamount.

significant vertical energy transfer. As before, however, the final surface cyclone is small, with significant filamentation. Over the seamount the cyclones merge successfully and the deep field is markedly weaker than with a basin.

In these cases, the cyclones are drawn together over a seamount, even with separations up to 5 times the vortex radius (figure 19). In contrast, vortices separated by more than 3 radii are expelled over a basin. The same effect has been seen in turbulence experiments, where anticyclones experience mutual attraction over a basin but not cyclones (LaCasce *et al.* 2024). In those experiments, the asymmetric attraction led to the formation of a lone anticyclone over basins and a lone cyclone over seamounts.

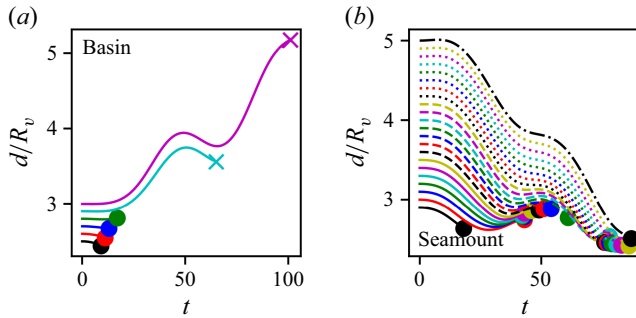


Figure 19. Evolution of the relative distance d/R_v between the centres of the two cyclonic vortices with $R_v = R_d$ for horizontally offset vortices and (a) a circular basin, (b) a circular seamount.

3.4.4. Bathymetry height and radius

Changing the topographic slope alters the initial strength of the deep anomalies, as inferred from (3.8). Changing the slope also impacts baroclinic instability, for example over a planar slope (LaCasce 1998). In the present cases the slope is altered both by the bathymetric height and its width. Thus we conducted additional experiments varying both, using the axisymmetric Gaussian bathymetry.

The results indicate that both effects are important. Increasing the height while holding the width fixed led to more rapid mergers over seamounts and slower mergers over basins. In some cases, where the cyclones would merge over a basin for a given slope, they would be ejected when the slope was doubled. The more rapid merger over seamounts with steeper slopes illustrates how the deep anomalies generated by the initial flow alter the mutual approach. The anomalies are stronger when the slopes are steeper. Similarly, the deep tripole generated over a basin by instability is stronger with steeper slopes, and the satellite anticyclones force the surface cyclones away. On the other hand, if the basin is shallow enough, the cyclones can merge and even persist as a single vortex. This is the case for example for $\Delta R = 2R_v$ and $\alpha_b h_0 = -0.5q_0$ and keeping $R_v = R_d$ and $R_b = 3R_d$, corresponding to $\beta_t = -0.5$.

Increasing the radius R_b for a fixed height, h_0 , has an additional effect, *viz.* increasing the horizontal range over which vortices can merge. This is in line with the experiments over an elliptical bathymetry, where the critical merger distance was increased along the major axis. Thus, for example, with $\Delta R = 2R_v$ and $R_b = 1.5R_d$ and keeping $\alpha_b h_0 = -q_0$, $R_v = R_d$, the cyclones merged and a portion of the final vortex persisted.

Thus it is the strength of the topographic slope which dictates the evolution. Thus smaller features with reduced amplitudes can produce comparable surface perturbations to larger, higher structures. But the bathymetric features must still exceed deformation scale.

3.4.5. Surface-trapped flow

In QG turbulence simulations (LaCasce *et al.* 2024) and observations (de La *et al.* 2016; Ni *et al.* 2023), surface vortices have weak or zero flow at the bottom in the presence of bathymetry. The vortices considered thus far have zero PV at the bottom initially and so do have deep flow. This results in the generation of anomalies, as described in (§ 3.2). This effect is absent if the initial vortices are compensated.

Thus we conducted additional experiments with $\varphi_2 = 0$ at $t = 0$. Then the initial surface and bottom PVs are

$$q_1 = \nabla^2 \varphi_1 - \gamma_1^2 \varphi_1, \quad q_2^a = \gamma_2^2 \varphi_1. \quad (3.12)$$

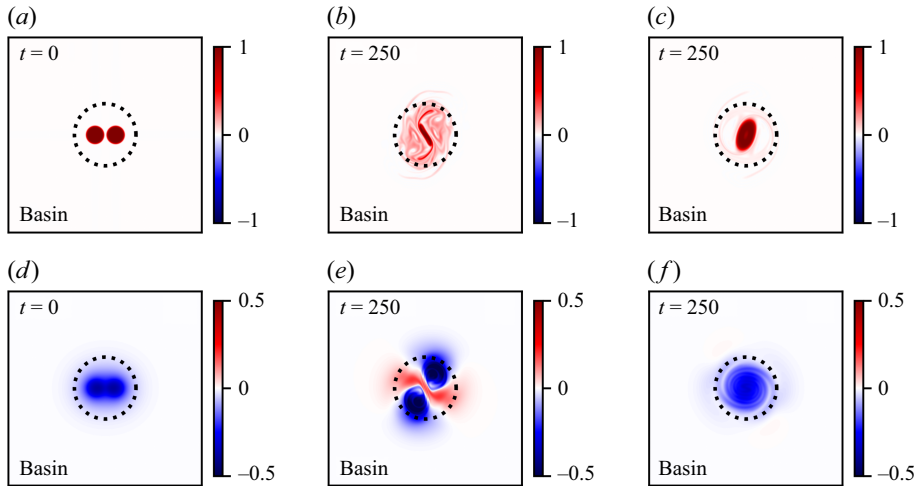


Figure 20. Potential vorticity anomalies with $\Delta R = 2R_v$ and $R_v = R_d$ with $\varphi_2(t=0) = 0$. Top row: q_1 for (a) a circular basin/seamount at $t = 0$, (b) a circular basin at $t = 250$, (c) a circular seamount at $t = 250$. Bottom row: q_2^a for (d) a circular basin/seamount $t = 0$, (e) circular basin at $t = 250$, (f) a circular seamount at $t = 250$.

Note that q_2^a at $t = 0$ is independent of the bathymetry. With two cyclonic vortices in the upper layer, there are corresponding negative PV anomalies ($q_2^a < 0$) at depth (figure 20d). This dipolar structure replaces the quadrupole seen early on in the previous experiments (e.g. figure 4d).

Over both the basin and seamount, the vortices merge. An example, with $\Delta R = 2R_v$, is shown in figure 20. As before, the cyclones experience strong filamentation while the anticyclones do not. An energetic tripole forms again over the basin, but the deep flow under the anticyclone is dominated by a single cyclone. The latter follows the merging of the two initial cyclonic anomalies. Unlike the surface anticyclone, the deep cyclone largely follows the isobaths. The counter-clockwise circulation is prograde and thus consistent with the mean flow predicted by Bretherton & Haidvogel (1976) and Salmon *et al.* (1976).

Interestingly, the merger characteristics are much more similar than with $q_2^a(t=0) = 0$ (figure 21). With ΔR less than the critical separation, the distance decreases at early times and more slowly than over a flat bottom. But with larger separations, ΔR increases for both the basin and seamount while still decreasing with a flat bottom. Thus the primary difference between the basin and seamount is the robustness and size of the merged vortex.

While the present experiments were conducted with equal layer depths, additional experiments indicate that increasing the bottom-layer depth yields qualitatively similar results, albeit with some weakening of the bathymetric influence (not shown). Thus, in much of the ocean, where the surface layer is typically 4–5 times shallower than the deep ocean, one would still expect merger asymmetry over the bathymetry.

4. Summary and discussion

The present study confirms that mergers of cyclonic surface vortices are favoured over a seamount and thus anticyclonic vortices are favoured over basins. Interacting cyclones over a basin are disrupted, yielding extensive filamentation and smaller vortices. The effect pertains to deformation-scale vortices or larger; mergers between smaller vortices are

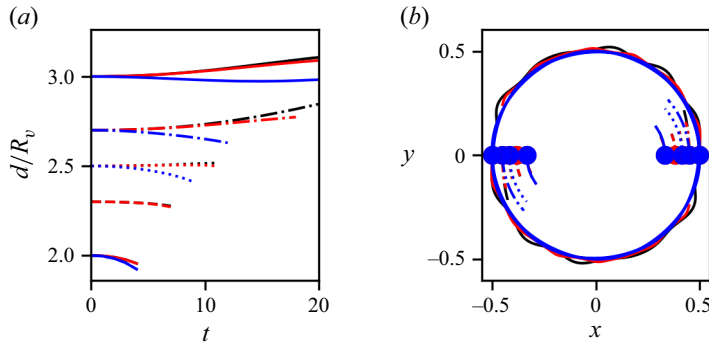


Figure 21. (a) Evolution of the distance between the vortex centres with an initially surface-trapped flow, for a basin (black), a seamount (red), a flat bottom (blue), with various $\Delta R/R_v = d(t=0)/R_v$. (b) Trajectory of the vortex centres in the upper layer until they merge, using the same colours as in (a).

largely the same over bathymetry. The results do not depend on the initial alignment of the vortices with the bathymetry nor whether the vortices are compensated, and similar results are obtained with unequal layer depths.

The primary factor behind the asymmetric mergers is the baroclinic instability of cyclones over basins (and anticyclones over seamounts) (Benilov 2005; Zhao *et al.* 2019). The fastest growing mode has an azimuthal wavenumber of 2, observed in these experiments as an intensifying quadrupole at depth. The deep PV anomalies which form resemble topographic waves in that they have zero PV in the upper layer. However, they do have surface flow and as such can disrupt the upper-layer vortices. The strength of the surface flow depends on the horizontal scale of the deep anomalies and is only substantial if the scale exceeds the deformation radius. As such, the instability is reminiscent of that in Eady's model (Eady 1949), where (density) anomalies on the upper and lower surfaces fail to interact when smaller than deformation scale. Eady waves have zero PV in the fluid interior and have a vertical extent identical to that of topographic waves. In Eady's model, the baroclinic instability has a short-wave cutoff whereby modes with wavenumbers exceeding a critical wavenumber, k_c , proportional to the inverse Rossby deformation radius, are stable.

At finite amplitude the deep anomalies evolve to a tripole structure in a basin, with a cyclonic central vortex and two satellite anticyclones. In some cases the latter couple with surface cyclones to form baroclinic modons or 'hetons' (Flierl *et al.* 1980; Hogg & Stommel 1985), resulting in the expulsion of the cyclones from the basin. The central deep cyclone is left behind. As such, this fundamental interaction – the baroclinic instability of a surface cyclone over a basin – may be an important factor in the generation of deep cyclonic circulation in a basin and the expulsion of surface cyclones. The deep flow is predicted by a minimum enstrophy calculation in two layers (LaCasce *et al.* 2024), but the mechanism for the formation has been unclear until now. The vertical energy transfer may also be important in terms of the global energy balance, by moving energy from the surface to the bottom where it can be dissipated (Wunsch & Ferrari 2004).

The present results help explain the frequent and puzzling appearance of lone surface anticyclones over submarine basins, both in ocean observations (e.g. the Lofoten vortex in the Nordic Seas; Köhl 2007; Sjøiland & Rossby 2013; Bosse *et al.* 2019; Trodahl *et al.* 2020b) and in baroclinic turbulence experiments (Solodoch *et al.* 2021; LaCasce *et al.* 2024). It was speculated previously that anticyclonic vortices congregate over basins due to self-advection, as isolated barotropic anticyclones experience a ' β -drift'

toward deeper water just as such vortices drift southwards on the planetary β -plane (e.g. McWilliams & Flierl 1979; Carnevale *et al.* 1991*b*; Zavala Sansón *et al.* 2012). Such self-propulsion results from the generation of secondary ‘ β -gyres’ which act back on the primary vortex (McWilliams & Flierl 1979). The same can occur in two layers if the vortex has a sufficiently strong bottom flow (LaCasce 1998). However, the surface vortices in these experiments have very weak or zero bottom flow. Indeed, mergers favour a surface anticyclone over a basin even when the surface vortices are initially compensated (§ 3.4.5). Thus, it is unlikely that anticyclones like the Lofoten vortex self-propel toward deeper water. Simulations (e.g. Trodahl *et al.* 2020*a* and LaCasce *et al.* 2024) suggest vortices of both signs spread off away from the continental shelf and out into the Lofoten basin; the anticyclones merge with the central vortex while the cyclones are sheared out. Thus it is the merger asymmetry and baroclinic stability, both of which favour anticyclones, that are the most likely explanations.

LaCasce *et al.* (2024) speculated that merger asymmetry favours anticyclones over a basin. Cyclones were observed to enter and leave the basin without merging while anticyclones merged. The effect commenced only after the vortices reached deformation scale; prior to that, mergers between cyclones and anticyclones were comparable. The present experiments confirm this asymmetry. We have also seen that cyclones tend to be expelled over basins. In the experiments with initially offset vortices (§ 3.4.3), the generation of intense deep anticyclones beneath the surface cyclones led to the formation of baroclinic dipoles (‘hetons’). These subsequently propagated out of the domain. This gives yet another reason to expect anticyclones over a basin rather than cyclones.

While isolated, quasi-stationary anticyclones are frequently observed at the ocean surface over basins, quasi-stationary cyclones are not seen over seamounts. This is likely because the bathymetry must exceed deformation scale in extent. Such seamounts are rare. One might expect surface cyclones over a submarine mountain range, like the mid-Atlantic Ridge, but observations thus far are lacking.

Isolated anticyclones are also observed over basins in barotropic turbulence, where baroclinic instability is absent (Solodoch *et al.* 2021; Siegelman & Young 2023; LaCasce *et al.* 2024). However, isolated cyclones are also unstable over a basin in a single layer fluid (Gonzalez & Zavala Sansón 2023). Therefore, the merger asymmetry also applies evidently to single layer systems and is related to vortex stability.

As noted, QG turbulence experiments with sufficiently steep bathymetry yield surface vortices with near zero bottom flow (LaCasce *et al.* 2024). However, oceanic vortices frequently do have deep flow, for example in the Lofoten basin (Bashmachnikov *et al.* 2017; Bosse *et al.* 2019; Trodahl *et al.* 2020*a*) and elsewhere (Ni *et al.* 2023). While the present experiments yield qualitatively similar merger asymmetry for vortices with zero deep flow, it is the simulations with zero deep PV which most closely resemble the turbulence simulations in LaCasce *et al.* (2024). Thus the zero deep PV condition may well be more relevant for oceanic vortices than compensation.

The present work focused on the QG evolution of the flow. The study of the influence of gravity waves induced by the interaction between the flow and the bathymetry is a possible extension. Such interactions likely enhance further the transfer of energy from the surface mesoscale features to depth.

Acknowledgements. We are grateful to three anonymous reviewers for constructive criticism of the manuscript.

Declaration of interest. The authors report no conflict of interest.

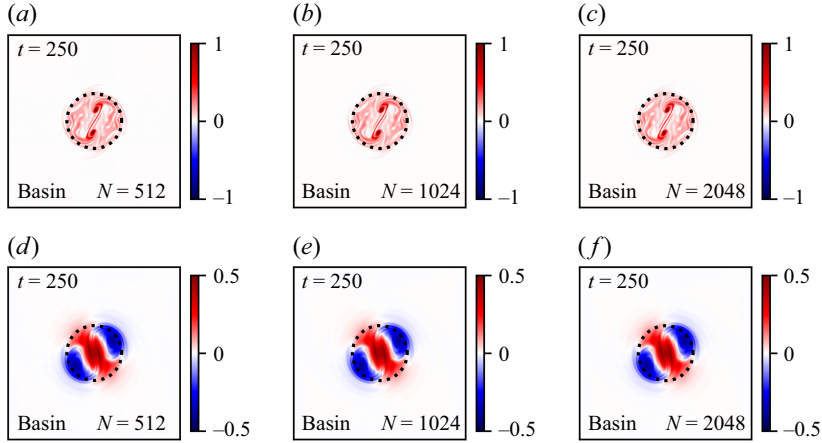


Figure 22. Potential vorticity anomalies at $t = 250$ for deformation-scale vortices ($R_v = R_d$) with an initial separation of $\Delta R = 2R_v$ as in figure 2(b,e) at three resolutions of $N = 512, 1024$ and 2048 .

Appendix A. Resolution and numerical convergence

The computational domain is doubly periodic in the horizontal with normalised dimensions L^2 , where $L = 6\pi R_d = 2\pi$, with $N = 2^n$ points in each direction. All fields are represented by their truncated Fourier series. We denote with k the wavenumber in the x -direction and l the wavenumber in the y -direction. The Fourier coefficient of any field a corresponding the wavenumber pair (k, l) is denoted $\hat{a}_{k,l}$. Simulations are performed using $N = 1024 = 2^{10}$ unless otherwise stated.

Equations (2.1), (2.2) become

$$\hat{q}_{1,k,l} = -(k^2 + l^2 + \gamma^2)\hat{\phi}_{1,k,l} + \gamma^2\hat{\phi}_{2,k,l}, \quad (\text{A1})$$

$$\hat{q}_{2,k,l} - \alpha_b \hat{h}_b \equiv \hat{q}_{2,k,l}^a = -(k^2 + l^2 + \gamma^2)\hat{\phi}_{2,k,l} + \gamma^2\hat{\phi}_{1,k,l}, \quad (\text{A2})$$

a set of simultaneous linear equations which can be explicitly inverted to find $\hat{\phi}_{i,k,l}$ from $\hat{q}_{i,k,l}$, $i = 1, 2$. We have checked the influence of the grid resolution on the results. To that purpose we compare three simulations of the same flow at increasing resolutions $N = 512, 1024, 2048$. The flow simulated consists in a pair of cyclonic vortices ($q_0 > 0$) over a basin. The two vortices are sheared by the flow induced in the bottom layer, creating a large number of small-scale features. Figure 22 shows the upper- and lower-layer PV fields q_1 and q_2^a at $t = 250$. They are remarkably similar for such a highly complex flow, developing fine-scale structures. This indicates that using $N = 1024$ is enough to achieve high accuracy while limiting the computational cost of the simulations. An analysis of the evolution extrema of q_2^a over the domain is indistinguishable on a graph (not shown). Separate tests using both $N = 512$ and $N = 1024$ for a pair of vortices with $\Delta R = 0$ over a basin showed that results are very little affected by an increase in the CFL coefficient K from 0.1 up to 0.5 (results not shown). This confirms that our main simulations using $K = 0.1$ are very well resolved in time.

Appendix B. Linear stability of a single vortex

In the limit $\epsilon \rightarrow 0$, the perturbation of the PV contours leads to a perturbation of the PV field

$$q'_1(r, \theta, t) = \epsilon \text{Re} \left(\eta_1(t) e^{i(m\theta - \sigma t)} \right) \delta(r - \bar{r}_1), \quad (\text{B1})$$

$$q_2^{a'}(r, \theta, t) = \sum_{i=1}^{N_t} \epsilon \text{Re} \left(\eta_{2,i}(t) e^{i(m\theta - \sigma t)} \right) \delta(r - \bar{r}_{2,i}), \quad (\text{B2})$$

where δ is the Dirac distribution

$$\frac{Dr_1}{Dt} = \epsilon \frac{\text{DRe} \left(\eta_1 e^{i(m\theta - \sigma t)} \right)}{Dt} = v_1, \quad (\text{B3})$$

$$\frac{Dr_{2,i}}{Dt} = \epsilon \frac{\text{DRe} \left(\eta_{2,i} e^{i(m\theta - \sigma t)} \right)}{Dt} = v_{2,i}, \quad (\text{B4})$$

where v_1 and $v_{2,i}$ are the radial velocities which can be obtained by contour integration. Linearising with respect to ϵ , we obtain the eigenvalue problem

$$\left(\sigma - \frac{m\bar{u}_1}{\bar{r}_1} \right) \eta_1 = q_0 \eta_1 \mathcal{K}(\bar{r}_1, \bar{r}_1) + \Delta q_2 \sum_{j=1}^{N_t} \eta_{2,j} \mathcal{K}(\bar{r}_1, \bar{r}_{2,j}), \quad (\text{B5})$$

$$\left(\sigma - \frac{m\bar{u}_{2,j}}{\bar{r}_{2,i}} \right) \eta_{2,i} = q_0 \eta_1 \mathcal{K}(\bar{r}_{2,i}, \bar{r}_1) + \Delta q_2 \sum_{j=1}^{N_t} \eta_{2,j} \mathcal{K}(\bar{r}_{2,i}, \bar{r}_{2,j}), \quad (\text{B6})$$

where σ is the eigenvalue, $(\eta_1, \eta_{2,i})$ the eigenvector, \bar{u}_1 and $\bar{u}_{2,a}$ are the azimuthal velocities at the contours from the basic state, e.g. of the unperturbed vortex of the upper layer, and $\mathcal{K}(r, s)$ gives the influence of the contour at radius s on the contour at radius r . To obtain \mathcal{K} we define the barotropic PV anomaly perturbation q'_t and the baroclinic PV anomaly perturbation q'_c as in § 3.2

$$q'_t = \frac{q'_1 + q'_2}{2}, \quad q'_c = \frac{q'_1 - q'_2}{2}, \quad (\text{B7})$$

and their associated barotropic and baroclinic streamfunctions

$$\varphi'_t = \frac{\varphi'_1 + \varphi'_2}{2}, \quad \varphi'_c = \frac{\varphi'_1 - \varphi'_2}{2}, \quad (\text{B8})$$

$$\varphi'_1 = \varphi'_t + \varphi'_c, \quad \varphi'_2 = \varphi'_t - \varphi'_c. \quad (\text{B9})$$

Following Flierl (1988), the corresponding barotropic and baroclinic influence functions \mathcal{K} for the azimuthal mode m are given by

$$\mathcal{K}_t(r, s) = \begin{cases} -\frac{1}{2} \left(\frac{r}{s} \right)^{1+m}, & r < s, \\ -\frac{1}{2} \left(\frac{r}{s} \right)^{1-m}, & r \geq s, \end{cases} \quad (\text{B10})$$

for the barotropic part and by

$$\mathcal{K}_c(r, s) = \begin{cases} -m \frac{r}{s} K_m(\gamma^* s) I_m(\gamma^* r), & r < s, \\ -m \frac{r}{s} K_m(\gamma^* r) I_m(\gamma^* s), & r \geq s, \end{cases} \quad (\text{B11})$$

for the baroclinic part, where I_m and K_m are the m th-order modified Bessel functions of the first and second kinds, respectively.

REFERENCES

- BAMBREY, R.R., REINAUD, J.N. & DRITSCHER, D.G. 2007 Strong interactions between two co-rotating quasi-geostrophic vortices. *J. Fluid Mech.* **592**, 117–133.
- BASHMACHNIKOV, I.L., SOKOLOVSKIY, M.A., BELONENKO, T.V., VOLKOV, D.L., ISACHSEN, P.E. & CARTON, X. 2017 On the vertical structure and stability of the Lofoten vortex in the Norwegian Sea. *Deep-Sea Res. I Oceanogr. Res. Papers* **128**, 1–27.
- BENILOV, E.S. 2005 Stability of a two-layer quasigeostrophic vortex over axisymmetric localized topography. *J. Phys. Oceanogr.* **35** (1), 123–130.
- BOSSE, A., FER, I., LILLY, J.M. & SØILAND, H. 2019 Dynamical controls on the longevity of a non-linear vortex : the case of the Lofoten Basin Eddy. *Sci. Rep. UK* **9** (1), 13448.
- BRETHERTON, F.P. & HAIDVOGEL, D.B. 1976 Two-dimensional turbulence above topography. *J. Fluid Mech.* **78** (1), 129–154.
- BRINK, K.H. 1990 On the generation of seamount-trapped waves. *Deep Sea Res. A Oceanogr. Res. Papers* **37** (10), 1569–1582.
- BYRNE, D., MÜNNICH, M., FRENGER, I. & GRUBER, N. 2016 Mesoscale atmosphere ocean coupling enhances the transfer of wind energy into the ocean. *Nat. Commun.* **7**, ncomms11867.
- CARNEVALE, G.F., KLOOSTERZIEL, R.C. & VAN HEIJST, G.J.F. 1991a Propagation of barotropic vortices over topography in a rotating tank. *J. Fluid Mech.* **233**, 119–139.
- CARNEVALE, G.F., KLOOSTERZIEL, R.C. & VAN HEIJST, G.J.F. 1991b Propagation of barotropic vortices over topography in a rotating tank. *J. Fluid Mech.* **233**, 119–139.
- CARTON, X. 2001 Hydrodynamical modeling of oceanic vortices. *Surv. Geophys.* **22** (3), 179–263.
- CARTON, X., CIANI, D., VERRON, J., REINAUD, J. & SOKOLVSKIY, M. 2016 Vortex merger in surface quasi-geostrophy. *Geophys. Astrophys. Fluid Dyn.* **110** (1), 1–22.
- CARTON, X., MAZE, G. & LEGRAS, B. 2002 A two-dimensional vortex-merger in an external strain field. *J. Turbul.* **3**, N45.
- CARTON, X., MORVAN, M., REINAUD, J.N., SOKOLOVSKIY, M.A., L'HÉGARET, P. & VIC, C. 2017 Vortex merger near a topographic slope in a homogeneous rotating fluid. *Regular Chaotic Dyn.* **22** (5), 455–478.
- CERRETTELLI, C. & WILLIAMS, C.H.K. 2003 The physical mechanism for vortex merger. *J. Fluid Mech.* **475**, 44–77.
- CHELTON, D.B., SCHLAX, M.G. & SAMELSON, R.M. 2011 Global observations of nonlinear mesoscale eddies. *Prog. Oceanogr.* **91**, 167–216.
- DRITSCHER, D.G. 1995 A general theory for two-dimensional vortex interactions. *J. Fluid Mech.* **293**, 269–303.
- DRITSCHER, D.G. 2002 Vortex merger in rotating stratified flows. *J. Fluid Mech.* **455**, 83–101.
- EADY, E.T. 1949 Long waves and cyclone waves. *Tellus* **1**, 33–52.
- FLIERL, G.R., LARICHEV, V.D., MCWILLIAMS, J.C. & REZNIK, G.M. 1980 The dynamics of baroclinic and barotropic solitary eddies. *Dyn. Atmos. Oceans* **5**, 1–41.
- FLIERL, G.R. 1988 On the instability of geostrophic vortices. *J. Fluid Mech.* **197**, 349–388.
- GONZALEZ, J.F. & ZAVALA SANSÓN, L. 2023 Linear stability of monopolar vortices over isolated topography. *J. Fluid Mech.* **959**, A23.
- GROOMS, I., NADEAU, L.-P. & SMITH, K.S. 2013 Mesoscale eddy energy locality in an idealized ocean model. *J. Phys. Oceanogr.* **43** (9), 1911–1923.
- HAIDVOGEL, D.B., BECKMANN, A., CHAPMAN, D.C. & LIN, R.-Q. 1993 Numerical simulation of flow around a tall isolated seamount. Part iii: Resonant generation of trapped waves. *J. Phys. Oceanogr.* **23** (11), 2373–2391.
- VON HARDENBERG, J., MCWILLIAMS, J.C., PROVENZALE, A., SHCHPETKIN, A. & WEISS, J.B. 2000 Vortex merging in quasi-geostrophic flows. *J. Fluid Mech.* **412**, 331–353.
- HERBETTE, S., MOREL, Y. & ARHAN, M. 2003 Erosion of a surface vortex by a seamount. *J. Phys. Oceanogr.* **33**, 1664–1679.
- HIDENORI, A., XIAOMING, Z. & GREATBATCH, R.J. 2016 Energetics of the global ocean: the role of mesoscale eddies. In *World Scientific Series on Asia-Pacific Weather and Climate*, chap. 4, pp. 109–134. World Scientific.
- HOGG, N.G. & STOMMEL, H.M. 1985 The heton, an elementary interaction between discrete baroclinic geostrophic vortices, and its implications concerning eddy heat-flow. *Proc. R. Soc. Lond. A Math. Phys. Sci.* **397**, 1–20.
- HOGG, N.S. 1973 On the stratified Taylor column. *J. Fluid Mech.* **58** (3), 517–537.
- KÖHL, A. 2007 Generation and stability of a quasi-permanent vortex in the Lofoten Basin. *J. Phys. Oceanogr.* **37** (11), 2637–2651.

- DE LA, L., SANCHEZ, M., LACASCE, J.H. & FUHR, H.K. 2016 The vertical structure of ocean eddies. *Dyn. Stat. Clim. Syst.* **1**, dzw001.
- LACASCE, J.H. 1998 A geostrophic vortex over a slope. *J. Phys. Oceanogr.* **28**, 2362–2381.
- LACASCE, J.H., PALÓCZY, A. & TRODAHL, M. 2024 Vortices over bathymetry. *J. Fluid Mech.* **979**, A32.
- DE MAREZ, C., CARTON, X., MORVAN, M. & REINAUD, J.N. 2017 The interaction of two surface vortices near a topographic slope in a stratified ocean. *Fluids* **2** (4), 57.
- DE MAREZ, C., LE CORRE, M. & GULA, J. 2021 The influence of merger and convection on an anticyclonic eddy trapped in a bowl. *Ocean Model.* **167**, 101874.
- MCWILLIAMS, J.C. & FLIERL, G.R. 1979 On the evolution of isolated, nonlinear vortices. *J. Phys. Oceanogr.* **9** (6), 1155–1182.
- MERRYFIELD, W.J. 1998 Effects of stratification on quasi-geostrophic inviscid equilibria. *J. Fluid Mech.* **354**, 345–356.
- MEUNIER, P., EHRENSTEIN, U., LEWEKE, T. & ROSSI, M. 2002 A merging criterion for two-dimensional co-rotating vortices. *Phys. Fluids* **14**, 2757–2766.
- NI, Q., ZHAI, X., LACASCE, J.H., CHEN, D. & MARSHALL, D.P. 2023 Full-depth Eddy kinetic energy in the global ocean estimated from altimeter and Argo observations. *Geophys. Res. Lett.* **50**, e2023GL103114.
- OVERMAN, E.A. & ZABUSKY, N.J. 1982 A merging criterion for two-dimensional co-rotating vortices. *Phys. Fluids* **25**, 1297–1305.
- OZURGURLU, E., REINAUD, J.N. & DRITSCHER, D.G. 2008 Interaction between two quasi-geostrophic vortices of unequal potential-vorticity. *J. Fluid Mech.* **59**, 395–414.
- PETERSEN, M., WILLIAMS, S., MALTRUD, M., HECHT, M. & HAMANN, B. 2013 A three-dimensional eddy census of a high-resolution global ocean simulation. *J. Geophys. Res. Oceans* **118**, 1759–1774.
- POLVANI, L., ZABUSKY, N.J. & FLIERL, J. 1989 Two-layer geostrophic vortex dynamics. Part 1. Upper-layer V-states and merger. *J. Fluid Mech.* **205**, 215–242.
- REINAUD, J.N. 2017 The interaction of two co-rotating quasi-geostrophic vortices in the vicinity of a surface buoyancy filament. *Geophys. Astrophys. Fluid Dyn.* **112** (2), 130–155.
- REINAUD, J.N. & DRITSCHER, D.G. 2005 The critical merger distance between two co-rotating quasi-geostrophic vortices. *J. Fluid Mech.* **522**, 357–381.
- REINAUD, J.N. & DRITSCHER, D.G. 2018 The merger of geophysical vortices at finite Rossby and Froude number. *J. Fluid Mech.* **848**, 388–410.
- ROBERTS, K.V. & CHRISTIANSEN, J.P. 1972 Topics in computational fluid mechanics. *Comp. Phys. Commun.* **3** (Suppl. 1), 14–32.
- ROSSOW, V.J. 1977 Convective merging of vortex cores in lift generated wakes. *J. Aircraft* **14** (3), 283–290.
- SAFFMAN, P.G. & SZETO, R. 1980 Equilibrium shapes of a pair of equal uniform vortices. *Phys. Fluids* **23** (12), 2339–2342.
- SALMON, R., HOLLOWAY, G. & HENDERSHOTT, M.C. 1976 The equilibrium statistical mechanics of simple quasi-geostrophic models. *J. Fluid Mech.* **75** (4), 691–703.
- SIEGELMAN, L. & YOUNG, W.R. 2023 Two-dimensional turbulence above topography: vortices and potential vorticity homogenization. *Proc. Natl Acad. Sci. USA* **120** (44), e2308018120.
- SØILAND, H. & ROSSBY, T. 2013 On the structure of the Lofoten Basin Eddy. *J. Geophys. Res. Oceans* **118** (9), 4201–4212.
- SOKOLOVSKIY, M.A. & VERRON, J. 2014 *Dynamics of Vortex Structures in a Stratified Rotating Fluid. Atmospheric and Oceanographic Sciences Library*, vol. 47. Springer.
- SOLODOCH, A., STEWART, A.L. & MCWILLIAMS, J.C. 2021 Formation of anticyclones over topographic depressions. *J. Phys. Oceanogr.* **51**, 207–227.
- TRIELING, R.R., DAM, C.E.C. & VAN HEIJST, G.J.F. 2010 Dynamics of two identical vortices in linear shear. *Phys. Fluids* **22**, 117104.
- TRODAHL, M., ISACHSEN, P.E., LILLY, J.M., NILSSON, J. & KRISTENSEN, N.M. 2020a The regeneration of the Lofoten vortex through vertical alignment. *J. Phys. Oceanogr.* **50** (9), 2689–2711.
- TRODAHL, M., ISACHSEN, P.E., LILLY, J.M., NILSSON, J. & MELSOM KRISTENSEN, N. 2020b The regeneration of the Lofoten vortex through vertical alignment. *J. Phys. Oceanogr.* **50** (9), 2689–2711.
- VALLIS, G.K. 2006 *Atmospheric and Oceanic Fluid Dynamics: Fundamentals and Large-Scale Circulation*. Cambridge University Press.
- VENAILLE, A. 2012 Bottom-trapped currents as statistical equilibrium states above topographic anomalies. *J. Fluid Mech.* **699**, 500–510.
- WUNSCH, C. & FERRARI, R. 2004 Vertical mixing, energy, and the general circulation of the oceans. *Annu. Rev. Fluid Mech.* **36**, 281–314.
- ZAVALA SANSÓN, L. 2010 Solutions of barotropic trapped waves around seamounts. *J. Fluid Mech.* **661**, 32–44.

- ZAVALA SANSÓN, L., BARBOSA AGUIAR, A.C. & VAN HEIJST, G.J.F. 2012 Horizontal and vertical motions of barotropic vortices over a submarine mountain. *J. Fluid Mech.* **695**, 173–198.
- ZAVALA SANSÓN, L. & GONZALEZ, J.L. 2021 Travelling vortices over mountains and the long-term structure of the residual flow. *J. Fluid Mech.* **922**, A33.
- ZHAO, B., CHIEUSSE-GÉRARD, E. & FLIERL, G. 2019 Influence of bottom topography on vortex stability. *J. Phys. Oceanogr.* **39**, 3199–3219.